AIP Journal of Applied Physics

Quantum confinement of excitons in wurtzite InP nanowires

K. Pemasiri, H. E. Jackson, L. M. Smith, B. M. Wong, S. Paiman, Q. Gao, H. H. Tan, and C. Jagadish

Citation: Journal of Applied Physics **117**, 194306 (2015); doi: 10.1063/1.4921109
View online: http://dx.doi.org/10.1063/1.4921109
View Table of Contents: http://scitation.aip.org/content/aip/journal/jap/117/19?ver=pdfcov
Published by the AIP Publishing

Quantum confinement of excitons in wurtzite InP nanowires

K. Pemasiri,[1] H. E. Jackson,[1] L. M. Smith,[1] B. M. Wong,[2] S. Paiman,[3] Q. Gao,[3] H. H. Tan,[3] and C. Jagadish[3]
[1]*Department of Physics, University of Cincinnati, Cincinnati, Ohio 45221, USA*
[2]*Department of Chemical and Environmental Engineering and Materials Science, University of California, Riverside, California 92521, USA*
[3]*Department of Electronic Materials Engineering, Research School of Physics and Engineering, The Australian National University, Canberra, ACT 0200, Australia*

(Received 28 September 2014; accepted 3 May 2015; published online 19 May 2015)

Exciton resonances are observed in photocurrent spectra of 80 nm wurtzite InP nanowire devices at low temperatures, which correspond to transitions between the A, B, and C valence bands and the lower conduction band. Photocurrent spectra for 30 nm WZ nanowires exhibit shifts of the exciton resonances to higher energy, which are consistent with finite element calculations of wavefunctions of the confined electrons and holes for the various bands. © *2015 AIP Publishing LLC*.
[http://dx.doi.org/10.1063/1.4921109]

I. INTRODUCTION

Understanding how to harness bottom-up fabrication of III–V semiconductor nanowires for device applications requires an understanding of how their energy band structure is modified by their physical structure[1–5] The optical properties of these devices depend on the internal electronic symmetry of the bands, the quantum confinement of the electrons and holes and their Coulomb interaction, and also on the interaction of the incoming and outgoing electromagnetic field with the dielectric nanowire.[6] Here, we study the electronic band structure of wurtzite InP nanowires at low temperatures using polarized photocurrent spectroscopy. The diameter of the nanowires range from ~8 times the exciton Bohr radius down to ~2 times the Bohr radius. This is an important regime where the quantum confinement becomes noticeable (larger than the exciton binding energy), and yet effective mass theory can still provide important insights. Theoretical calculations have shown that for NW diameters smaller than the Bohr radius, full pseudopotential calculations are essential to calculate the effective band structure,[7] and Coulomb enhancements (dielectric confinement) can no longer be avoided.[8] The measurements described here thus provide an important first step towards understanding how these effects present themselves in smaller nanowires.

InP nanowires have been grown using Vapor-Liquid-Solid techniques with both cubic zincblende (ZB, the bulk structure symmetry) and hexagonal wurtzite (WZ) crystal structure as well as with controlled and uncontrolled mixed ZB/WZ homostructures.[9–12] The reduced symmetry in Wurtzite (hexagonal) NWs from Zincblende (cubic) NWs has a dramatic impact on the band structure and optical selection rules.[13–18] Two conduction bands appear instead of one, and three valence bands (A, B, and C) instead of two (degenerate light and heavy hole and split off bands). The splitting between the hole bands depends on the combination of the spin orbit interaction and the crystal field energy.[14,16,17,19] In this work, we study the properties of single (or a few) nanowire devices with single phase WZ crystal structure. Clear excitonic-like resonances are seen in low temperature (10 K) photocurrent (PC) spectra, which are consistent with these changes. In small diameter WZ nanowires, we show that the PC spectra can provide a direct measure of the quantum confinement of excitons, which is sensitive to the hole mass associated with the A, B, or C bands.

II. SAMPLES AND EXPERIMENTAL METHODS

InP nanowires were grown using the vapor-liquid-solid method with gold nanoparticles as catalysts on (111)B-oriented InP substrates at 400 °C using a metal-organic chemical-vapor deposition system. The WZ NWs were grown using 20 nm catalysts with a V/III ratio of 700.[9] Paiman *et al.* have shown that at such a growth temperature, the higher V/III ratio leads dominantly to WZ nanowires, while the lower V/III ratio tends to grow dominantly ZB nanowires, with some twins and stacking faults present as determined by high-resolution transmission electron microscopy imaging.[9] CW and time-resolved photoluminescence measurements of these nanowires have confirmed the ZB and WZ nature of the nanowires.[13,19] While most of the WZ NWs were ~25 nm in diameter, occasionally larger diameter NWs were observed most likely because of aggregation of the gold catalyst during the growth process.

To isolate single nanowires for device fabrication, the NWs were first mechanically transferred from the InP growth substrate to a small piece of Si substrate, which was then sonicated in a methanol solution to create a very dilute distribution of nanowires. A droplet containing a dilute solution of these nanowires was dispersed onto a second Si substrate, which had a 300 nm thermally grown SiO_2 insulating layer to facilitate fabrication of the electrical contacts. The Si/SiO_2 substrate was spun with a standard photoresist and was then positioned under an optical mask having large 200 μm openings separated by 1–5 μm gaps to define the NW contacts. By observing through the large openings in the mask, a nanowire could be positioned so that contact windows could be exposed using a Karl Suss MJB3 mask aligner. After

development, the substrate was immersed in an ammonium polysulfide solution under a 60 W white light for 30 min to etch off the oxide layer around the nanowire. This procedure helps to improve the Ohmic contact formation between the metal-semiconductor interfaces. Similar techniques have been used by several groups to make Ohmic contact with semiconductor materials including InAs, GaAs, and AlGaAs.[20] Standard metal deposition and lift off techniques were then used to fabricate 200 nm Ti/Al contact pads across the nanowire separated by a $\sim 4\,\mu$m gap. Gold wires were then wire bonded to the large metal contacts of the nanowire device after mounting on a chip carrier.

The NW device in its package was then mounted onto the cold finger of a continuous flow liquid He cryostat, and the device was observed through a thin window using a long working distance 10× or 50× microscope objective. For photocurrent spectroscopy, the nanowire was broadly illuminated with a tunable (700–1000 nm) CW Ti-Sapphire laser, which was mechanically chopped at a frequency of 137 Hz.[21] The laser spot size was $\sim 30\,\mu$m, and the incident average power was kept below 5 μW. The photocurrent signal was measured using a digital lock-in amplifier with the gain and time-constants adjusted so as to maintain the same signal to noise.

The WZ InP nanowires studied here were largely 25 nm in diameter as shown in the TEM image in Fig. 1; occasionally, however, larger diameter wires (50–100 nm) were also observed. One device studied was fabricated from a larger ~80 nm WZ InP nanowire, while a second device had two 30 nm diameter WZ InP nanowires spanning the Ti/Al contacts as seen in the SEM image of an actual device shown in the bottom of Fig. 1.

III. PHOTOCURRENT SPECTRA

Figure 2(a) shows an unpolarized photocurrent spectrum of the larger diameter (80 nm) WZ InP device, which displays three peaks at 1.504, 1.530, and 1.655 eV associated with transitions between the A, B, and C valence bands and the conduction band. We interpret these peaks as due to the increased oscillator strength of exciton resonances, since band-to-band transitions observed at higher temperatures show only the onset of the density of states.[22,23] These transitions are the same as those seen in photoluminescence excitation spectra published by Perera *et al.*[13,14] and also

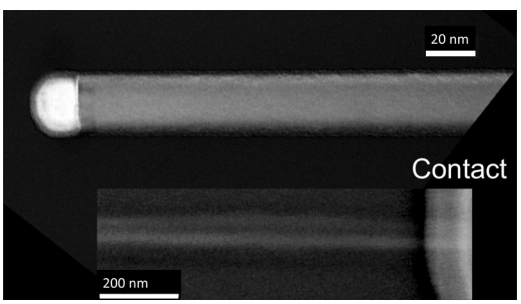

FIG. 1. TEM micrograph of a WZ InP nanowire of diameter ~26 nm. A 20 nm gold catalyst can be seen at the end of the nanowire. SEM micrograph (inset) of the nanowire device D2 having two WZ InP nanowires of diameter ~30 nm.

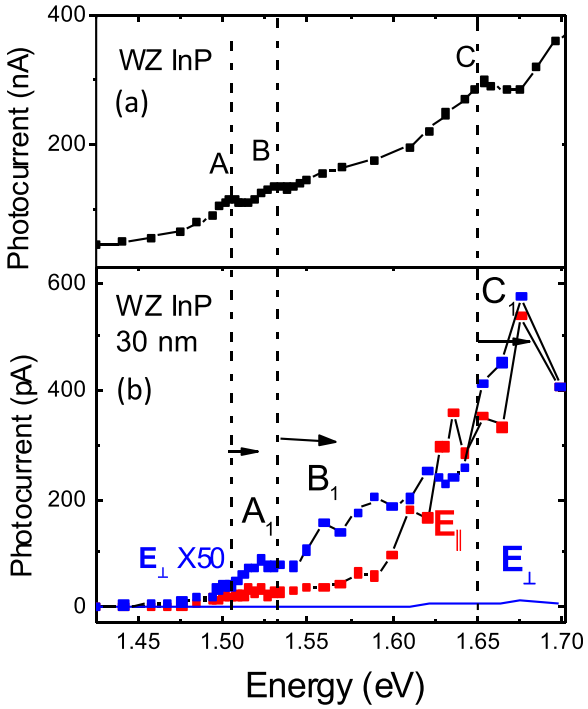

FIG. 2. Photocurrent spectra of WZ InP nanowire devices. (a) Unpolarized photocurrent spectrum of ~80 nm NW device, showing excitonic-like peaks A, B, and C at energies of ~1.504 eV, ~1.531 eV, and ~1.653 eV, respectively. (b) Polarized spectra from ~30 nm NW device. Solid blue line shows perpendicular photocurrent, and red squares shows parallel photocurrent. Blue squares show perpendicular photocurrent magnified by a factor of 50. Excitonic-like peaks A, B, and C are shifted to higher energies to ~1.523 eV, ~1.575 eV, and ~1.675 eV, respectively, at 10 K. The vertical dashed lines refer to the A, B, and C position of the large NW device, while the horizontal arrows shows the relative shift of A, B, and C excitonic states.

reported by others.[16] The splitting between the three hole bands is determined by combination of the spin-orbit interaction and the crystal field energy.[14,16,17]

Fig. 2(b) shows polarized PC spectra from the device with two small 30 nm diameter WZ InP NWs. The photocurrent spectrum for laser excitation parallel to the wire is nearly 50 times larger than for laser excitation polarized perpendicular to the NW. While transitions from the A valence band to conduction band should be only allowed for electric fields polarized perpendicular to the c-axis (the NW long axis),[18,19] such effects are masked for a high dielectric constant semiconductor nanowire ($R \ll \lambda$), since for perpendicularly polarized light the internal electric field, E_i, is reduced from the incident (external) field strength, E_e, by the dielectric contrast $Ei = (2\ \varepsilon_0/(\varepsilon + \varepsilon_0))\ E_e$.[6] For an InP NW where $\varepsilon = 12.4$, the photocurrent for perpendicular light should be only 2% that for the parallel case, consistent with the measurement here. Polarization effects due to the band symmetries have been observed in extremely tapered (non-symmetric) Wurtzite InP NWs, where the dielectric effects are substantially reduced.[18,19] Interestingly, the exciton resonances in the photocurrent are seen more clearly in Fig. 2(b) for perpendicular polarization, perhaps indicating that band-to-band transitions are suppressed substantially relative to the exciton resonance. Recent experiments have shown substantial perpendicular polarization for both A and B hole transitions with the conduction band.[18]

The perpendicular photocurrent shows distinct shifts of the A, B, and C exciton resonances to higher energies, suggestive of quantum confinement of the electrons and holes, but also shows significant additional structure for both parallel and perpendicular polarized PC spectra in the energies between the B and C resonances, which are not present in the larger WZ NW device. The positions marked by the arrows in Fig. 2(b) show the energy transitions expected for the ground state wavefunctions for electrons and holes confined to a 30 nm hexagonally symmetric (WZ) nanowire as we will now discuss.

IV. CALCULATIONS OF QUANTUM CONFINED STATES

To provide a more accurate picture of the electronic states confined to the 30 nm diameter NW, we have used finite element calculations to determine the quantum eigenstates for all three valence bands and the lowest conduction band in a hexagonally symmetric WZ InP nanowire. We use a modified version of the customized finite element code described in more detail by Wong *et al.*[24] The single particle electron and hole wavefunctions are calculated as a linear combination of Bloch wavefunctions in the single band model, and Coulomb effects between electrons and holes are not included. As noted by Wang *et al.*, in this diameter range (30 nm) complex pseudopotential and simple effective mass approximations yield the same results.[7] The effective electron and hole masses used are the well understood values for ZB InP: $m_e = 0.08$, $m_A = m_{HH} = 0.6$, $m_B = m_{LH} = 0.089$, and $m_C = m_{SO} = 0.16$. For each calculation, a very dense grid of nearly 35 000 triangular elements was used to accurately describe the localized and oscillatory wavefunctions. The vertex-to-vertex distance was used as a free parameter to fit the prominent transition energies observed in the photocurrent spectra that correspond to transitions between the ground hole states A_1, B_1, and C_1 and the ground electron state e_1. The best fit was obtained for a vertex-to-vertex distance of 31.4 nm (or a flat-to-flat distance of 27 nm).

The wavefunctions and energies, which result from this procedure, are shown in Fig. 3. A ladder of states is observed, which are of two types: single states such as the ground state and excited states that are hexagonally symmetric with only radial nodes, and a series of states that show an increasing number of angular nodes. Using solutions to the cylindrically symmetric states as a closely related model, we find that these states can be characterized using two quantum numbers: n, which reflects the number of radial nodes, and m, which reflects the increasing number of angular nodes. While the orbital angular momentum is not expected to be a good quantum number in the hexagonal case (as it is for a cylindrical nanowire), the states have a very similar symmetry. The ground state is therefore $(n,m) = (1,0)$, with a series of two degenerate excited state doublets corresponding to $(n,m) = (1,\pm1)$ and $(1,\pm2)$ before the single hexagonally symmetric excited state $(n,m) = (2,0)$ appears at higher energy. Interestingly, the $(n,m) = (1,\pm3)$ states, which are hexagonally symmetric are not degenerative because in one case, the carriers are localized to the corners, while the other (higher energy) state are localized to the edges. This complex ladder of states occurs for each of the electron and three hole bands, and their confinement energies are shown in the table on the right side of Fig. 3.

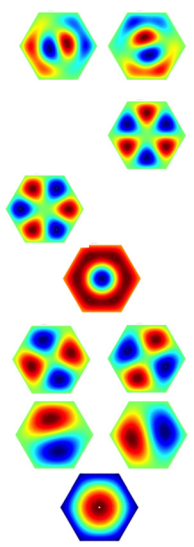

(n,m)	A (meV)	B (meV)	C (meV)	e (meV)
(2,±1)	15.5	104.5	68.7	116.2
(1,+3)	13.6	91.5	60.2	101.8
(1,-3)	12.3	82.8	54.4	92.1
(2,0)	9.7	65.1	42.8	72.5
(1,±2)	8.4	56.4	37.0	62.7
(1,±1)	4.7	31.5	20.7	35.0
(1,0)	1.8	12.4	8.2	13.8

FIG. 3. Left images show lowest ten wavefunctions calculated using finite element methods as described in the text. Table to the right shows confinement energies of A, B, and C valence bands and the lowest conduction band (e). The quantum number n reflects increasing radial nodes, and m reflects increasing angular nodes.

V. DISCUSSION AND SUMMARY

The magnitude of the polarized photocurrent shown in Fig. 2(b) increases by nearly two orders of magnitude for both parallel and perpendicular polarizations as the excitation energy increases from the band edge. In order to see the entire structure for both polarizations, we show in Fig. 4 both PC spectra on a log scale where the perpendicular polarized spectrum is multiplied by a factor of 80 so that it can be seen in the same plot as the parallel polarized spectrum. Using the calculated eigenstates above, we consider transitions only between electron and hole states, which have the same symmetry, and so are labeled only by the relevant hole state. Thus, the transitions labeled $A_{n,m}$ or $B_{n.m}$ reflect the optical transitions $A_{n,m} \rightarrow e_{n,m}$, $B_{n,m} \rightarrow e_{n,m}$, and so on. Transitions associated with $m = 0$ are shown by solid lines and are clearly seen in the linear spectra (Fig. 2(b)), while those associated with $m \neq 0$ are labeled with dashed lines and are not clearly seen in either spectra. As expected, prominent features are seen in the PC spectra for transitions between $A_{1,0}$, $B_{1,0}$, $C_{1,0}$, and $e_{1,0}$. In addition, an excited state transition is identified for $A_{2,0} \rightarrow e_{2,0}$, and the transition of $B_{2,0} \rightarrow e_{2,0}$ occurs at the same energy as $C_{1,0} \rightarrow e_{1,0}$, which may explain its substantial intensity. A series of poorly- or unresolved structure in the photocurrent are also seen in the energy region between $A_{2,0} \rightarrow e_{2,0}$ and $B_{2,0} \rightarrow e_{2,0}/C_{1,0} \rightarrow e_{1,0}$. While these may be related to transitions between hole and electron states where $m \neq 0$, we cannot at this time attribute the peaks to a particular electronic transition.

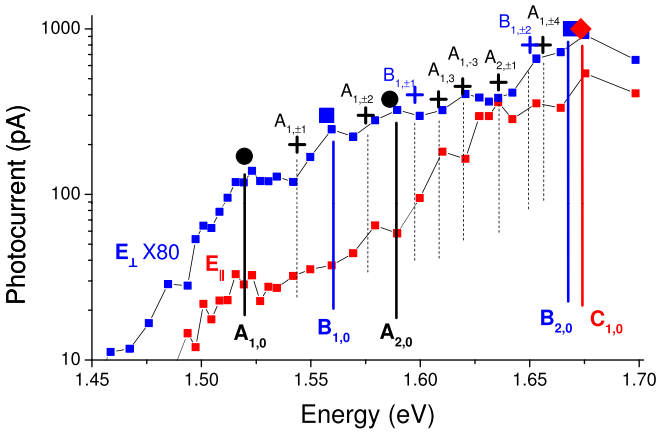

FIG. 4. Polarized photocurrent spectra from 30 nm device on a log scale. Blue squares show perpendicular polarized spectrum, while red squares show parallel polarized spectrum. The perpendicular photocurrents are multiplied by a factor of 80 to be seen on the same scale. Black circles and solid line show transition energies of $A_{1,0}\rightarrow e_{1,0}$ and $A_{2,0}\rightarrow e_{2,0}$ (see text). Blue squares and solid lines show transition energies of $B_{1,0}\rightarrow e_{1,0}$ and $B_{2,0}\rightarrow e_{2,0}$. Red diamond and solid line shows transition energy of $C_{1,0}\rightarrow e_{1,0}$. Dashed lines show transition energies of higher order states with angular nodes reflecting the ladder diagram in Fig. 3, but which are not clearly seen in the photocurrent spectra.

In summary, we have used polarized photocurrent spectroscopy to characterize the energy landscape of WZ InP nanowire Ohmic devices at low temperatures. At low temperatures (10 K), we observe pronounced excitonic resonances corresponding to the A, B, and C valence bands for WZ nanowires at energies consistent with recent PLE measurements in WZ nanowires.[13,14,16,18] In a ~30 nm WZ nanowire device, the A, B, and C exciton peaks are observed to be ~20 – 30 meV higher than in the larger diameter WZ InP device, consistent with quantum confinement effects. Finite element effective mass calculations of the quantum confined states in a hexagonally symmetric wire allow us to attribute resonances to both the ground states for the A, B, and C excitons as well as the excited state for the A and B excitons. Photocurrent measurements in smaller diameter nanowires should be highly informative, since the effective mass approximation should no longer be viable.

ACKNOWLEDGMENTS

We acknowledge the financial support of the National Science Foundation through Grant Nos. DMR-1105362, 1105121, and ECCS-1100489 and Australian Research Council. The Australian National Fabrication Facility is acknowledged for access to the growth facilities used in this research. B.M.W. acknowledges the National Science Foundation for supercomputing resources through the Extreme Science and Engineering Discovery Environment (XSEDE), Project No. TG-CHE130052.

[1]M. Fickenscher, T. Shi, H. E. Jackson, L. M. Smith, J. M. Yarrison-Rice, C. Zheng, P. Miller, J. Etheridge, B. M. Wong, Q. Gao, S. Deshpande, H. H. Tan, and C. Jagadish, Nano Lett. **13**, 1016–1022 (2013).
[2]H. J. Joyce, Q. Gao, H. Hoe Tan, C. Jagadish, Y. Kim, J. Zou, L. M. Smith, H. E. Jackson, J. M. Yarrison-Rice, P. Parkinson, and M. B. Johnston, Prog. Quantum Electron. **35**, 23–75 (2011).
[3]M. Montazeri, M. Fickenscher, L. M. Smith, H. E. Jackson, J. Yarrison-Rice, J. H. Kang, Q. Gao, H. H. Tan, C. Jagadish, Y. Guo, J. Zou, M.-E. Pistol, and C. E. Pryor, Nano Lett. **10**, 880–886 (2010).
[4]M. E. Reimer, G. Bulgarini, N. Akopian, M. Hocevar, M. B. Bavinck, M. A. Verheijen, E. P. A. M. Bakkers, L. P. Kouwenhoven, and V. Zwiller, Nat. Commun. **3**, 737 (2012).
[5]J. Wallentin, N. Anttu, D. Asoli, M. Huffman, I. Aberg, M. H. Magnusson, G. Siefer, P. Fuss-Kailuweit, F. Dimroth, B. Witzigmann, H. Q. Xu, L. Samuelson, K. Deppert, and M. T. Borgström, Science **339**, 1057–1060 (2013).
[6]H. E. Ruda and A. Shik, J. Appl. Phys. **100**, 024314 (2006).
[7]J. Wang, J.-W. Luo, L. Zhang, and A. Zunger, Nano Lett. **15**, 88–95 (2014).
[8]L. V. Keldysh, Phys. Status Solidi **164**, 3–12 (1997).
[9]S. Paiman, Q. Gao, H. H. Tan, C. Jagadish, K. Pemasiri, M. Montazeri, H. E. Jackson, L. M. Smith, J. M. Yarrison-Rice, X. Zhang, and J. Zou, Nanotechnology **20**, 225606 (2009).
[10]K. Pemasiri, M. Montazeri, R. Gass, L. M. Smith, H. E. Jackson, J. Yarrison-Rice, S. Paiman, Q. Gao, H. H. Tan, C. Jagadish, X. Zhang, and J. Zou, Nano Lett. **9**, 648–654 (2009).
[11]H. J. Joyce, J. Wong-Leung, Q. Gao, H. H. Tan, and C. Jagadish, Nano Lett. **10**, 908–915 (2010).
[12]K. A. Dick, P. Caroff, J. Bolinsson, M. E. Messing, J. Johansson, K. Deppert, L. R. Wallenberg, and L. Samuelson, Semicond. Sci. Technol. **25**, 024009 (2010).
[13]S. Perera, K. Pemasiri, M. A. Fickenscher, H. E. Jackson, L. M. Smith, J. Yarrison-Rice, S. Paiman, Q. Gao, H. H. Tan, and C. Jagadish, Appl. Phys. Lett. **97**, 023106 (2010).
[14]S. Perera, T. Shi, M. A. Fickenscher, H. E. Jackson, L. M. Smith, J. M. Yarrison-rice, S. Painam, G. Qiang, H. H. Tan, and C. Jagadish, Nano Lett. **13**, 5367 (2013).
[15]A. De and C. E. Pryor, Phys. Rev. B **81**, 155210 (2010).
[16]E. G. Gadret, G. O. Dias, L. C. O. Dacal, M. M. de Lima, C. V. R. S. Ruffo, F. Iikawa, M. J. S. P. Brasil, T. Chiaramonte, M. A. Cotta, L. H. G. Tizei, D. Ugarte, and A. Cantarero, Phys. Rev. B **82**, 125327 (2010).
[17]L. C. O. Dacal and A. Cantarero, Solid State Commun. **151**, 781–784 (2011).
[18]M. De Luca, A. Zilli, H. A. Fonseka, S. Mokkapati, A. Mitriametro, H. H. Tan, L. M. Smith, C. Jagadish, M. Capizzi, and A. Polimeni, Nano Lett. **15**, 998–1005 (2015).
[19]A. Mishra, L. V. Titova, T. B. Hoang, H. E. Jackson, L. M. Smith, J. M. Yarrison-Rice, Y. Kim, H. J. Joyce, Q. Gao, H. H. Tan, and C. Jagadish, Appl. Phys. Lett. **91**, 263104 (2007).
[20]N. Tajik, Z. Peng, P. Kuyanov, and R. R. LaPierre, Nanotechnology **22**, 225402 (2011).
[21]A. Maharjan, K. Pemasiri, P. Kumar, A. Wade, L. M. Smith, H. E. Jackson, J. M. Yarrison-Rice, A. Kogan, S. Paiman, Q. Gao, H. H. Tan, and C. Jagadish, Appl. Phys. Lett. **94**, 193115 (2009).
[22]R. Elliott, Phys. Rev. **108**, 1384–1389 (1957).
[23]W. Turner, W. Reese, and G. Pettit, Phys. Rev. **136**, A1467–A1470 (1964).
[24]B. M. Wong, F. Leonard, Q. Li, and G. T. Wang, Nano Lett. **11**, 3074–3079 (2011).